Angle-Resolved Photoemission Studies of Quantum Materials

Donghui Lu,[1] Inna M. Vishik,[2,4] Ming Yi,[2,5] Yulin Chen,[2] Rob G. Moore,[2] and Zhi-Xun Shen[2,3,4,5]

[1]SSRL and [2]SIMES, SLAC National Accelerator Laboratory, Menlo Park, California 94025; email: dhlu@slac.stanford.edu, zxshen@stanford.edu

[3]GLAM,[4]Department of Applied Physics, and [5]Department of Physics, Stanford University, Stanford, California 94305

Annu. Rev. Condens. Matter Phys. 2012. 3:129–67

First published online as a Review in Advance on January 3, 2012

The *Annual Review of Condensed Matter Physics* is online at conmatphys.annualreviews.org

This article's doi: 10.1146/annurev-conmatphys-020911-125027

1947-5454/12/0310-0129$20.00

Keywords

cuprates, pnictides, graphene, topological insulator, Fermi surface, band dispersion

Abstract

Angle-resolved photoemission spectroscopy (ARPES) has emerged as a leading experimental probe for studying the complex phenomena in quantum materials, a subject of increasing importance. The power of this technique stems from the directness and the richness of the momentum-resolved information it can provide, such as band dispersion, Fermi surface topology, and electron self-energy. Over the past decade, the significantly improved energy and momentum resolution and carefully matched experiments have turned this technique into a sophisticated tool in characterizing the electronic structure of complex materials. This revolution is mostly evident in the study of cuprate high-temperature superconductors. More recently, this technique has played a critical role in advancing our understanding of the newly discovered iron-based superconductors and topological insulators. In this paper we review some of the recent ARPES results and discuss the future perspective in this rapidly developing field.

1. INTRODUCTION

The investigation of "emergent phenomena" in quantum materials will be a major theme of condensed matter physics in the twenty-first century. As better controlled model systems become available, a sophisticated understanding of the universality and diversity of these quantum materials may lead to great revelations well beyond themselves. Understanding these novel quantum phenomena is crucial to the progress of fundamental science in the form of the modern theory of solids, as well as to the development of alternative pathways for the design of new materials and functional devices, which hold so much promise for technological advances. Angle-resolved photoemission spectroscopy (ARPES), due to its unique capability to directly probe the momentum-resolved electronic structure, can play a critical role in achieving a comprehensive understanding of these complex phenomena where momentum dependent anisotropy is important.

With the development of the latest generation of ultrahigh-resolution electron spectrometers, ARPES technique has experienced a renaissance in the past decade. The significantly improved energy and momentum resolution not only allow us to map out electronic structures, including band dispersions and Fermi surface (FS) topology, with unprecedented precision, but also make it possible to obtain important information on the electron self-energy, thereby turning it into a sophisticated tool for studying the strongly correlated systems. Nowhere is this revolution more evident than in the study of the high-temperature superconductors (HTSCs), which (more than two decades after their discovery) continue to defy theoretical explanation. More recently, the discovery of superconductivity in various iron-based superconductors with T_c as high as 55 K has generated another intensive wave of research in this field. In both cases, ARPES has played an important role in advancing our understanding of these novel superconductors by providing critical information on their underlying electronic structure, from which superconductivity emerges. Toward the ultimate goal of understanding the mechanism of high T_c superconductivity, ARPES can help us to address a number of key issues. Among them are

- Energy gap structure tied to the symmetry of the superconducting order parameter;
- Extraction of electron self energy for studying many-body correlation effects;
- Characterization of the doping evolution from the magnetic parent phase to the superconducting phase; and
- Understanding the nature of the competing electronic phases and their relationship to superconductivity, such as the pseudogap phase in cuprates and the spin-density-wave (SDW) state in pnictides.

In addition to high-temperature superconductivity, the other modern topic in the field of ARPES over the past few years is Dirac fermion physics, including both graphene and topological insulators (TIs). Graphene, a single sheet of carbon atoms densely packed in a honeycomb crystal lattice, has long been the subject of theoretical studies. Its exotic quantum electrodynamic properties arise from the presence of Dirac cones in the electronic structure, as recently demonstrated by ARPES measurements on graphene thin film. A TI, however, is a novel state of quantum matter predicted by theory that is topologically distinct from all other known states of matter. The most distinct feature in its electronic structure is a surface state with Dirac cone–like dispersion that resides inside the bulk insulating gap. This surface state is predicted to be protected by the time reversal symmetry (TRS) and immune to perturbations such as nonmagnetic impurities, but can open a gap at the Dirac node upon magnetic doping as the TRS is violated. ARPES, due to its advantage of probing both surface- and bulk-related electronic states, has played a leading role in the investigations of TIs. Soon after the theoretical

predictions, a number of TI systems have been experimentally confirmed and characterized by ARPES. These pioneering works not only pave the way to realize many exciting novel topological phenomena but also point to the direction toward controlling the topological surface state, which is crucial for turning this new state into applications, such as spintronics devices.

In this review, we first examine the recent progress in ARPES study of both cuprate and iron-based superconductors. For the second part, we highlight some of the ARPES results on graphene and TIs.

2. CUPRATE SUPERCONDUCTORS

The high-T_c superconducting cuprates have inspired intense research interest since their discovery in 1986. The cuprates consist of one or more copper-oxygen (CuO_2) layers, with the Cu atoms forming a square lattice, separated by charge reservoir layers. It has been established that most of the interesting physics occurs in the CuO_2 layers, and properties are tuned by changing the concentration of mobile electrons (*n*-type) or holes (*p*-type) there. Other phases appear in close proximity to superconductivity, including antiferromagnetism, spin glass, stripe order, and the pseudogap state (1–4), making these compounds complex manifestations of strongly-correlated-electron physics, but very fruitful manifestations nonetheless. A myriad of advances, including innovations in ARPES as well as other experimental techniques, the synthesis of increasingly high-quality samples, and the development of theoretical models have been motivated by the enormity of the cuprate challenge, and in turn these advances have propelled our understanding of cuprates. However, a key piece of information remains missing: a microscopic theory of the mechanism of high-temperature superconductivity. There are several logical approaches to the cuprate problem: (*a*) understanding the Mott insulator parent compound and how it evolves with doping; (*b*) studying coupling to bosonic modes that may be related to a pairing glue; and (*c*) understanding the normal state above T_c, which for the underdoped (UD) cuprates is the enigmatic pseudogap state. Most early ARPES studies on cuprates have been discussed previously (5). For this review, we discuss more recent progress since 2003. A number of research groups have contributed to the progress made, but we mostly focus on our own work here.

2.1. Mott Insulator and Lightly Doped State

The undoped parent compounds of the cuprates are strongly correlated antiferromagnetic (AFM) insulators, and understanding excitations in this state is a natural starting point for UD cuprates. An ideal system for this is $Ca_2CuO_2Cl_2$ (CCOC) because of its simple tetragonal, single CuO_2 layer crystal structure. **Figure 1*a,b*** show the energy distribution curves (EDCs) taken on CCOC near ($\pi/2$, $\pi/2$) for the lower Hubbard band (LHB), a strongly correlated band, and the O $2p_\pi$ band, a more conventional band (6). Both sets of EDCs are fit well by a Gaussian line shape with a width on the order of hundreds of millielectron volts, inconsistent with coherent quasiparticle (QP)-like excitations, which would yield EDCs with much sharper Lorentzian line shapes (5). A Gaussian line shape, however, is consistent with a Frank-Condon broadening scenario (7) having vanishingly small QP spectral weight, shown schematically in **Figure 1*c***. Frank-Condon broadening indicates strong coupling of electrons to a bosonic field. The fact that both the LHB and O $2p_\pi$ bands exhibit Frank-Condon broadening suggests that the responsible bosonic field is of lattice origin, namely polarons, rather than magnetic origin, because the O $2p_\pi$ states near (π, π) do not couple to low-energy spin excitations (8). Lattice polaron formation suggests that strong electron-phonon coupling is present even in the parent

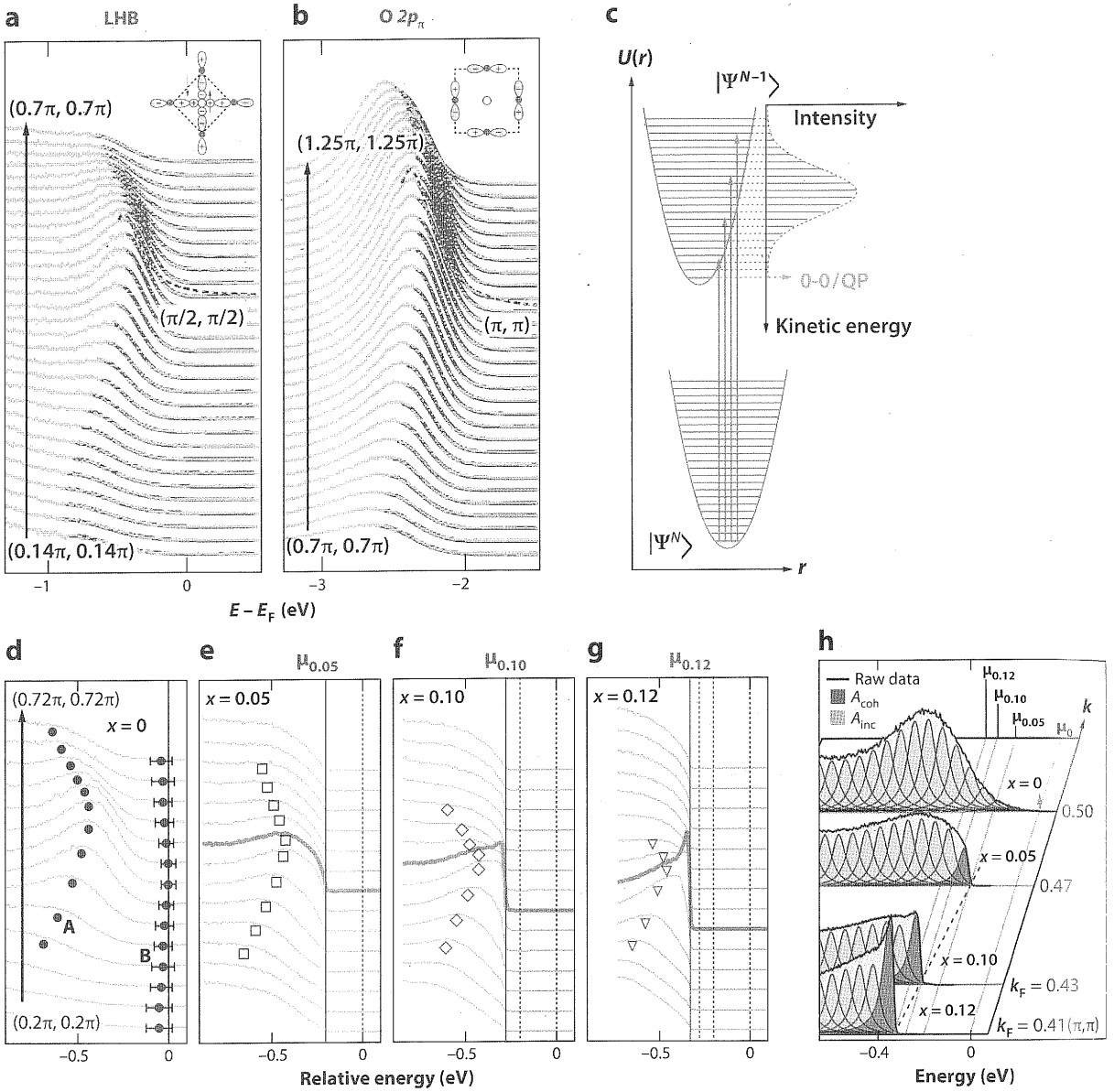

Figure 1

Frank-Condon broadening and chemical potential shift in $Ca_2CuO_2Cl_2$ (CCOC) and $Ca_{2-x}Na_xCuO_2Cl_2$ (Na-CCOC). (*a*, *b*) Energy distribution curve (EDC) taken around (π/2, π/2) and (π, π) on CCOC (6). Raw data are fit well by Gaussian peaks (*red*) but not Lorentzians (*purple dashed lines*). (*c*) Schematic of Frank-Condon process (7). (*d–g*) EDCs for Na-CCOC with $x = 0$, 0.05, 0.10, and 0.12, respectively, plotted on a relative energy scale to reflect the shift of μ with doping. Open symbols mark peak position of lower Hubbard band (LHB) (feature A), and filled symbols in panel *d* mark the 3σ onset of intensity (feature B), which sets the lower bound of μ for $x = 0$. (Data from Reference 9.) (*h*) Schematic of doping dependence at k_F showing the shift of μ and transfer of spectral weight from incoherent part (*pink*) to coherent part (*blue*) with hole doping. Abbreviation: QP, quasiparticle.

material, and coupling to lattice degrees of freedom needs to be considered in addition to expected magnetic ones. With hole doping, the QP peak first emerges along the (0,0) to (π,π) or nodal direction, as seen in $Ca_{2-x}Na_xCuO_2Cl_2$ (Na-CCOC) (9). In the undoped, insulating case, the chemical potential μ is ill-defined, but a lower bound is set by the onset of the LHB, defined as the 3σ signal of the Gaussian peak of the LHB. As doping increases, μ rigidly shifts down toward the LHB, as shown in **Figure 1*d–h***, and a QP peak becomes visible between $x = 0.05$ and $x = 0.10$, comprising a coherent low-energy band. Thus, the doping process from AFM insulator to metal (at least along the nodal direction) is described as a shift in μ, accompanied by a transfer of spectral weight from the incoherent (LHB) portion to the coherent (QP) portion of the spectrum. Analogous physics has been observed in other cuprate systems, as well as in the manganite compounds with colossal magnetoresistance, where ARPES studies along the nodal direction have found a transition from a polaronic insulator to a polaronic metal as QPs emerge below the Curie temperature (10).

2.2. Dispersion Anomalies

Cuprate dispersions near E_F are not smooth, but exhibited prominent dispersion anomalies, or kinks, the most studied of which is the ubiquitous kink found along the nodal direction at 50–80 meV (called the intermediate-energy kink in this review) (11–15). In multilayer cuprates, this kink persists all around the FS, giving rise to the famous peak-dip-hump (PDH) EDC line shape in the antinodal (AN) region (14, 16, 22). Early studies showed that the intermediate-energy kink along the nodal direction is present in many families of cuprates at different dopings and persists even above T_c (11, 16–18). Its energy scale is close to that of the superconducting gap maximum, making it an intriguing candidate to study in the context of pairing. The origin of this kink remains under debate, with strong coupling to phonons (16, 20) or magnetic excitations (17, 21) being the leading candidates, and some arguing that the dispersion anomalies at the node and AN may have different origins (22). Since our previous comprehensive review (5), we have demonstrated the ubiquity of dispersion anomalies at multiple energies in the cuprates and gained further understanding of the intermediate-energy kink by establishing its detailed systematic behavior as a function of temperature, doping, and number of CuO_2 planes in the unit cell. In addition, efforts have been made by other groups to study the oxygen isotope effect in order to shed light on the nature of the intermediate-energy kink (23, 24).

Two other dispersion anomalies are seen in the dispersions derived from momentum distribution curve (MDC) analysis, besides the intermediate-energy kink: the high-energy anomaly and the low-energy kink (**Figure 2**). The high-energy anomaly, or waterfall feature, appears at 300–500 meV, marked by the onset of a vertical dispersion, where the MDC peak position is independent of binding energy, as shown for $Bi_2Sr_2CuO_6$ (Bi2201), $Bi_2Sr_2CaCu_2O_8$ (Bi2212), $Ba_2Ca_3Cu_4O_8(O_\delta F_{1-\delta})_2$ (F0234), and $La_{2-x}Sr_xCuO_4$ (LSCO) (**Figure 2*a–d***). It has been observed in electron- and hole-doped cuprates (25) and below and above T_c. There have been multiple proposals for the origin of the high-energy anomaly, but it is most readily attributed to Mott-Hubbard physics, arising from the meeting of the incoherent LHB and the coherent QP bands, and this spectral weight leakage may lend insight into many-body physics in the cuprates (26).

The advent of laser ARPES (27) has revealed another kink at around 8–15 meV in the nodal dispersion of Bi2212 (**Figure 2*j–k***) (28–31). This kink is ubiquitous in UD Bi2212, evident in the MDC dispersion (28, 29, 31), the MDC width (28, 31), and the scattering rate derived from EDC analysis (30). It becomes stronger with underdoping, leading to a nodal Fermi velocity

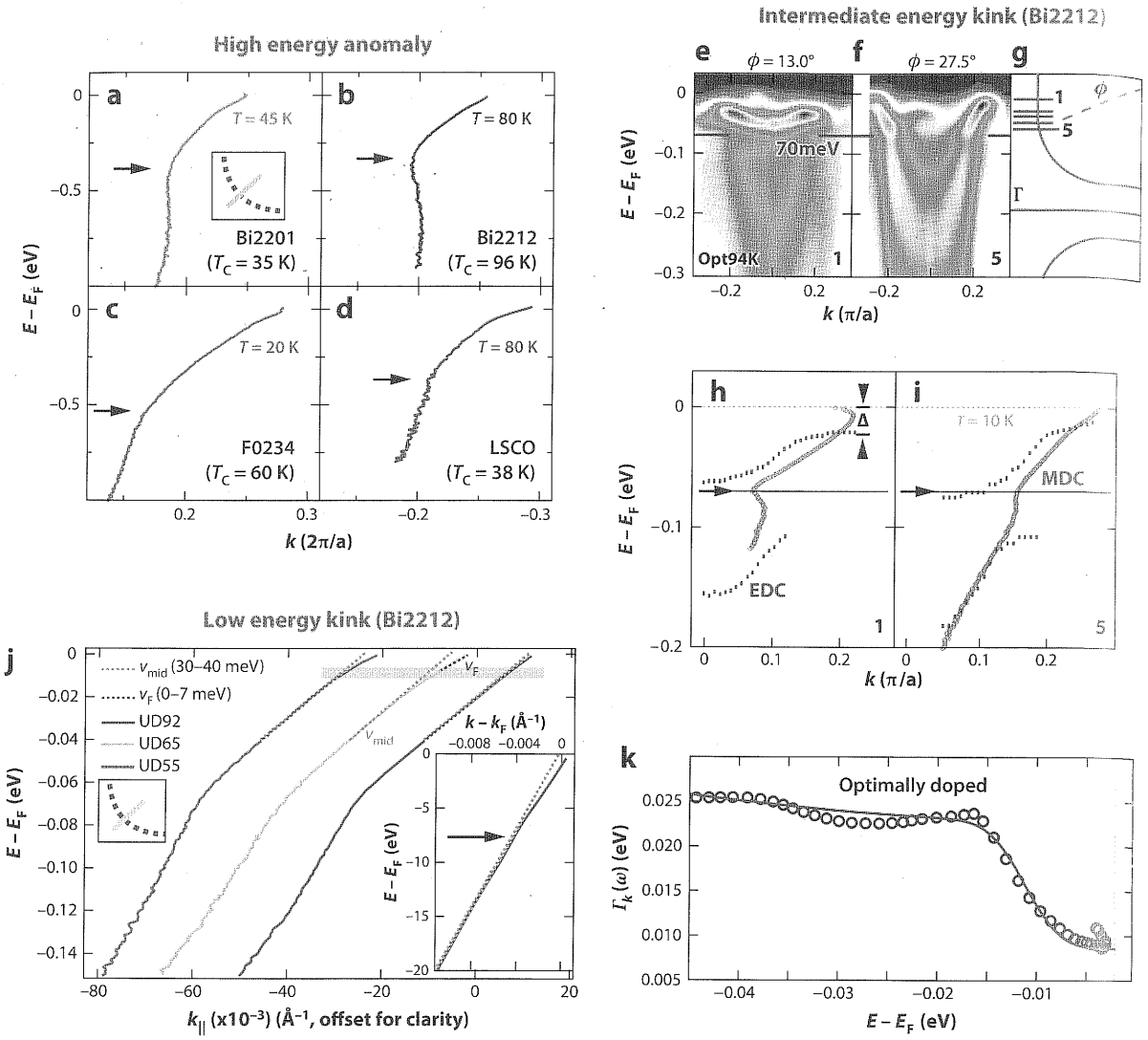

Figure 2

Hierarchy of kinks in cuprates. (*a–d*) High energy anomaly in nodal momentum distribution curve (MDC) dispersion (*black arrow*) is ubiquitous in cuprates at energy 300–500 meV (23). (*e–i*) Intermediate-energy kink, shown for optimally doped Bi2212 near the nodal and antinodal (AN) regions at 10 K (16). (*e,f*) Image plots at cut positions are shown in panel *g*, cut 1, in the AN, and in cut 5 in the nodal regions. (*h,i*) Energy distribution curve (EDC) and MDC peak positions showing dispersion anomaly near 70 meV. Δ in panel *h* denotes energy gap at cut position 1. In the AN region, the spectrum breaks into coherent and incoherent portions, giving rise to a peak-dip-hump line shape. (*j*) Low energy kink (10–15 meV) measured by laser ARPES in the nodal dispersion of Bi2212 (28). Gray bar marks approximate the kink energy where the slope of the dispersion measured within 7 meV of E_F (V_F) deviates from that measured between 30–40 meV (V_{mid}, *gray dotted line*). (*k*) A low-energy kink as seen as an anomaly in the scattering rate from an optimally doped Bi2212. (Reprinted with permission from Reference 30. Copyright 2009 by the American Physical Society.)

that decreases with underdoping, which has important implications for understanding transport experiments (28). Unlike other dispersion anomalies, the low-energy kink appears at an energy scale smaller than the maximum of the *d*-wave superconducting gap [~40 meV in optimally doped (OP) Bi2212], suggesting a different origin from the intermediate-energy kink,

such as coupling to an acoustic phonon with preferential coupling with small momentum transfer (32).

Having established a hierarchy of energy scales in the cuprates, we now turn to systematic measurements, including temperature, doping, and CuO_2-layer number dependence, which have been used to elucidate the origin of the intermediate-energy kink that turns out to have more than one component, at both the node and the AN region. At the node, this kink persists, though weakened, above T_c at the same apparent energy (11, 17). Fine structures in this kink were studied across T_c in OP Bi2212 (33), as shown in **Figure 3*a***. At low temperature, a single peak around 70 meV is seen in the real part of the self energy (ReΣ), but above T_c, a second subkink appears near 40 meV. By comparing to the temperature dependence of ReΣ in nonsuperconducting Bi2201, this change was attributed to a loss of superconductivity rather than purely thermal effects. Across T_c, the subkink structure evolves in a way consistent with the closing of the gap over a portion of the FS at T_c and can be reproduced by a simple Holstein model with multiple weighted modes (33). Coupling to multiple phonon modes is reasonable because both the B_{1g} buckling mode (~36 meV) and the oxygen breathing mode (~70 meV) are expected to have nonzero coupling at the node (20). Studies on LSCO have also shown that multiple modes may contribute to the intermediate-energy nodal kink (19).

The nodal intermediate-energy kink is present throughout the phase diagram, with the coupling strength increasing with underdoping (11), until the Mott insulator regime when a QP description is no longer accurate (6). On the overdoped (OD) side, quantitative changes in the kink are associated with emerging *c*-axis metallicity, as reported in Bi2201 by Meevasana et al. (35). In OD Bi2201, ReΣ is reduced by nearly a factor of two from its value at OP and is peaked sharply at 70–75 meV. Meanwhile, ReΣ at optimal doping has more weight at lower energy, near 30–60 meV, as shown in **Figure 3*b***. The Eliashberg function was extracted using maximum entropy method to quantify the relative weight of different modes at different dopings, which reveals additional weight at 40 and 50 meV for optimal doping that may be assigned to out-of-plane motion of planar oxygen (35).

At the AN, the dispersion in multilayer cuprates is strongly broken up into an incoherent and a coherent portion, giving rise to a characteristic PDH line shape in the EDC (16), as shown in **Figure 2*e,h***. As the PDH line shape disappears across T_c, the AN kink has been attributed to a magnetic origin in some proposals (22). Alternately, the PDH line shape has been attributed to coupling to a B_{1g} buckling phonon because it is absent in single-layer compounds where such coupling is expected to be considerably weaker (20). In Tl-based cuprates ($Tl_2Ba_2Ca_{n-1}Cu_nO_{2n+4}$, n = 1, 2, and 3), a spin-resonance mode has been observed in the single-layer compound (36), making it an ideal system to distinguish between the two proposals (34). Band dispersions in the superconducting state are shown at the node and AN for Tl-2201, Tl-2212, and Tl-1223 near OP in **Figure 3*c–h***. Although all compounds share the ubiquitous intermediate-energy nodal kink at the AN, the multilayer systems show the dispersion breaking up into coherent and incoherent branches, whereas the single-layer compound does not. This suggests much weaker electron-boson coupling in the latter, and favors the scenario that the AN kink arises primarily from coupling to a buckling phonon. Based on these systematic investigations of the temperature, doping, and layer-number dependence, it is rational to associate the intermediate-energy kink in both nodal and AN regions with strong coupling to multiple phonon modes, although it is possible to have an additional electronic effect associated with the superconducting gap opening near T_c. We also note that an oxygen isotope effect on the energy scale of the intermediate-energy kink has been reported (23, 24), providing additional support to the lattice origin of this kink. In addition, there is the low-energy kink in Bi2212, which can be ascribed to coupling to an acoustic phonon (32), as well as polaronic

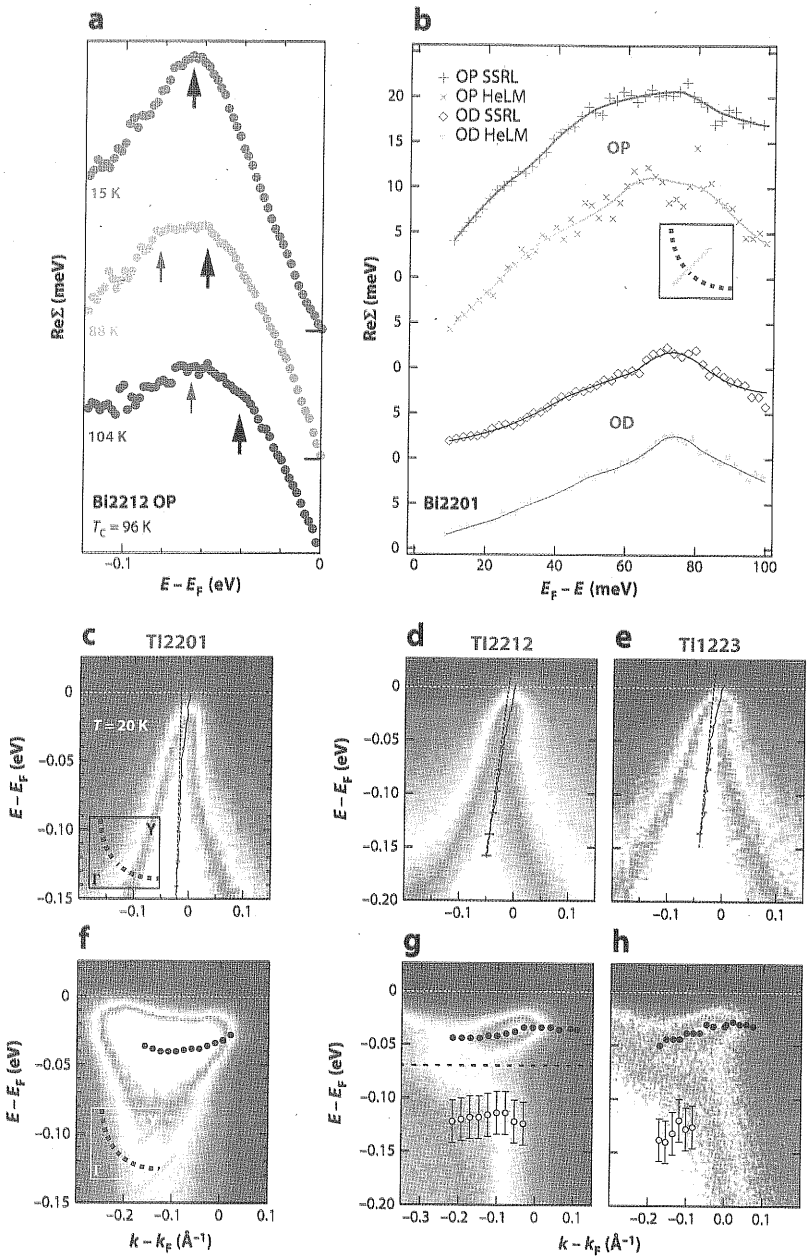

Figure 3

Temperature, doping, and layer number dependence of intermediate kink. (*a*) Temperature dependence evolution of nodal kink (33). A single feature at $\omega = 70$ meV for $T << T_c$ evolves into multiple features near and above T_c, which is attributed to the superconducting gap closing over a portion of the Fermi surface. (*b*) The real part of self energy (ReΣ) for $T > T_c$, for optimally doped (OP) and overdoped (OD) Bi2201 (35). (*c–e*) Nodal spectra with momentum distribution curve fittings at 20 K for Tl2201, Tl2212, and Tl2223, respectively (34). Nodal intermediate-energy kink does not show dependence on number of layers. (*f–h*) Antinodal spectra for the same compounds as in panels *c–e*. For Tl-based cuprates with two or more layers, the AN dispersion is split into two branches in panels *g* and *h*, shown by open (*filled*) circles corresponding to energy distribution curve peak (hump) positions, whereas for the single-layer compound it remains a single branch.

physics in the parent compound (6, 9). All of these results show that coupling between electrons and lattice manifest in multiple crucial ways throughout the phase diagram. How to think about these electron lattice interactions in the context of strong Coulomb and magnetic interactions is an interesting issue going forward.

2.3. Pseudogap and Superconducting Gap

One of the biggest challenges in the cuprates is to understand the normal state, especially the pseudogap state in the underdoped regime. The onset of the pseudogap at T^* has signatures in many different experiments (1, 37, 38), and in ARPES, it manifests as a partially gapped FS, with ungapped Fermi arcs near the node and an incoherent gap near the AN (39, 40). Interpretations of the pseudogap fall into two groups: preformed pairs ("one gap") (41, 42) and a state distinct from the superconducting state ("two gap"). In recent years, there has been increasing evidence for the latter scenario from doping, momentum, and temperature dependence studies using ARPES (43–46), and from other techniques with the capability for momentum-space discrimination, such as Raman scattering and scanning tunneling spectroscopy (47, 48).

Figure 4 summarizes key ARPES evidence for a two-gap picture. It has been observed that the gap function in UD cuprates in the superconducting state deviates from a simple *d*-wave form near the AN, as shown in **Figure 4*a***, with the deviation becoming stronger with decreasing hole concentration (43–45, 49). This deviation from a simple *d*-wave form suggests that something aside from superconductivity contributes to the spectral gap in the AN region below T_c, and the likely candidate is the pseudogap, which is strongest at the AN above T_c. Distinct features associated with both superconductivity and the pseudogap have been observed below T_c, providing further evidence of their coexistence (50, 51). This two-gap phenomenology was further unveiled through studying both the doping and temperature dependence of the gap structure in the nodal and AN regions. The AN gap increases with underdoping, following the established doping dependence of the pseudogap, but the near-nodal gap exhibits a different doping dependence, as shown in **Figure 4*b,c*** (43, 45). Also, the near-nodal gap closes at a temperature very close to T_c, as seen in raw and fitted data, whereas the AN gap persists above T_c (**Figure 4*d–g***). Thus, the gap in the AN region has a different doping and temperature dependence from the gap in the nodal region, which is inconsistent with the expected behavior of a single order parameter on a single FS. It is therefore more logical to associate the AN gap primarily with the pseudogap and the near-nodal gap primarily with the superconductivity. We note, however, that this dichotomy can be subtle, as superconducting QPs exist all around the FS in Bi2212 (52), and the crossover from one temperature-dependent behavior to another is not sharp. Nevertheless, this nodal/AN, superconductivity/pseudogap dichotomy reconciles the seemingly contradictory results on gap measurements from other techniques: Andreev reflection suggests that the gap closes at T_c (53), whereas scanning tunneling spectroscopy indicates that it remains unchanged across T_c (54). The former primarily probes nodal QPs, whereas the latter primarily measures AN states, so they can be consistent within a two-gap picture, where different order parameters dominate in different portions of the FS, as shown by ARPES.

More recent experiments on Pb-Bi2201 (55) have provided further insights into the possible origin of the pseudogap, as shown in **Figure 5**. Unlike Bi2212, this system lacks complications from bilayer splitting, and the superconducting feature is much weaker in the AN region, making it possible to isolate pseudogap effects. At $T>T^*$, the band in the AN region is metallic with a parabolic dispersion and well defined Fermi crossings (k_F). At $T<T_c$, however, spectra become much broader, and the back-bending position of the band, the momentum where the band dispersion is closest to E_F, does not coincide with k_F, as expected for superconducting

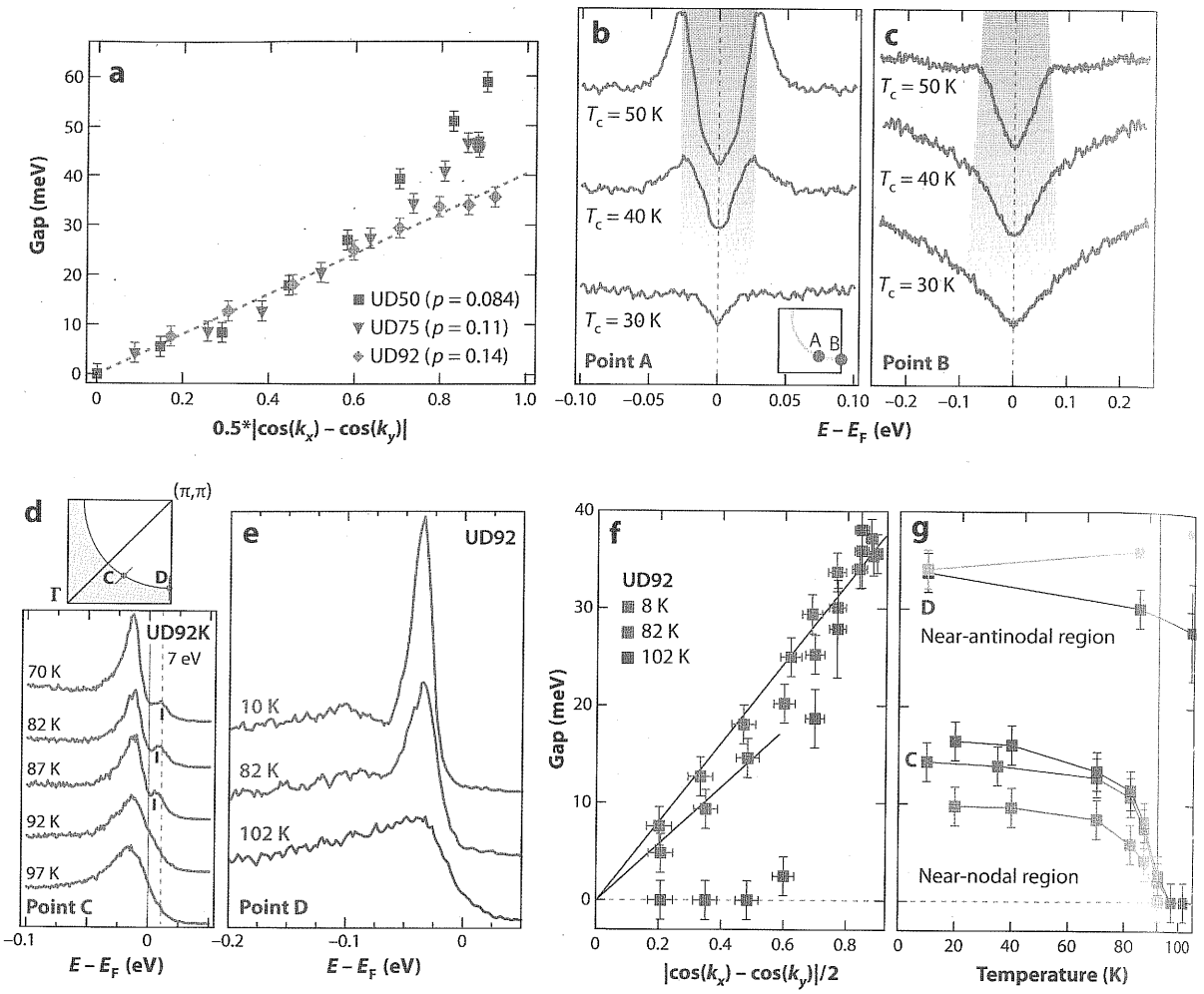

Figure 4

Two-gap phenomenology: momentum, doping, and temperature dependence in Bi2212. (*a*) Gap functions around the Fermi surface, plotted as a function of the simple *d*-wave form (44, 45), showing increasing deviation from a simple *d*-wave form near the AN region with increasing underdoping. (*b,c*) Symmetrized energy distribution curves (EDCs) at k_F in the near-nodal (NN) region (point A) and AN region (point B), showing different doping dependence of the gap (45). Approximate 2Δ highlighted by gray bar. (*d–g*) Different temperature dependence in different regions of momentum space for UD92 (44). EDCs in panel *d* show that the gap in the NN region closes near T_c, as the upper Bogoliubov peak at $\omega > E_F$ moves toward E_F. Meanwhile, the EDC peak position at the AN (*e*) does not change with temperature, though the sharp peak disappears above T_c. (*f*) Gap functions at three temperatures showing evolution from simple *d*-wave form at low temperature to a nodal Fermi arc and AN gap above T_c. (*g*) Temperature dependence of energy gaps at several momenta. In the NN region, the gap closes near T_c, whereas near the AN region, the gap remains mostly unchanged across T_c.

order where particle-hole symmetry dictates the alignment between k_F and back-bending position (**Figure 5*g,h***). However, a density wave order can reproduce the misalignment between k_F and the back-bending position (**Figure 5*i,j***), and a short-range order with multiple domains may reproduce the anomalous spectral broadening seen at low temperature (**Figure 5*k***). The gap, as defined by the EDC peak position at k_F, decreases with temperature and goes to zero at the

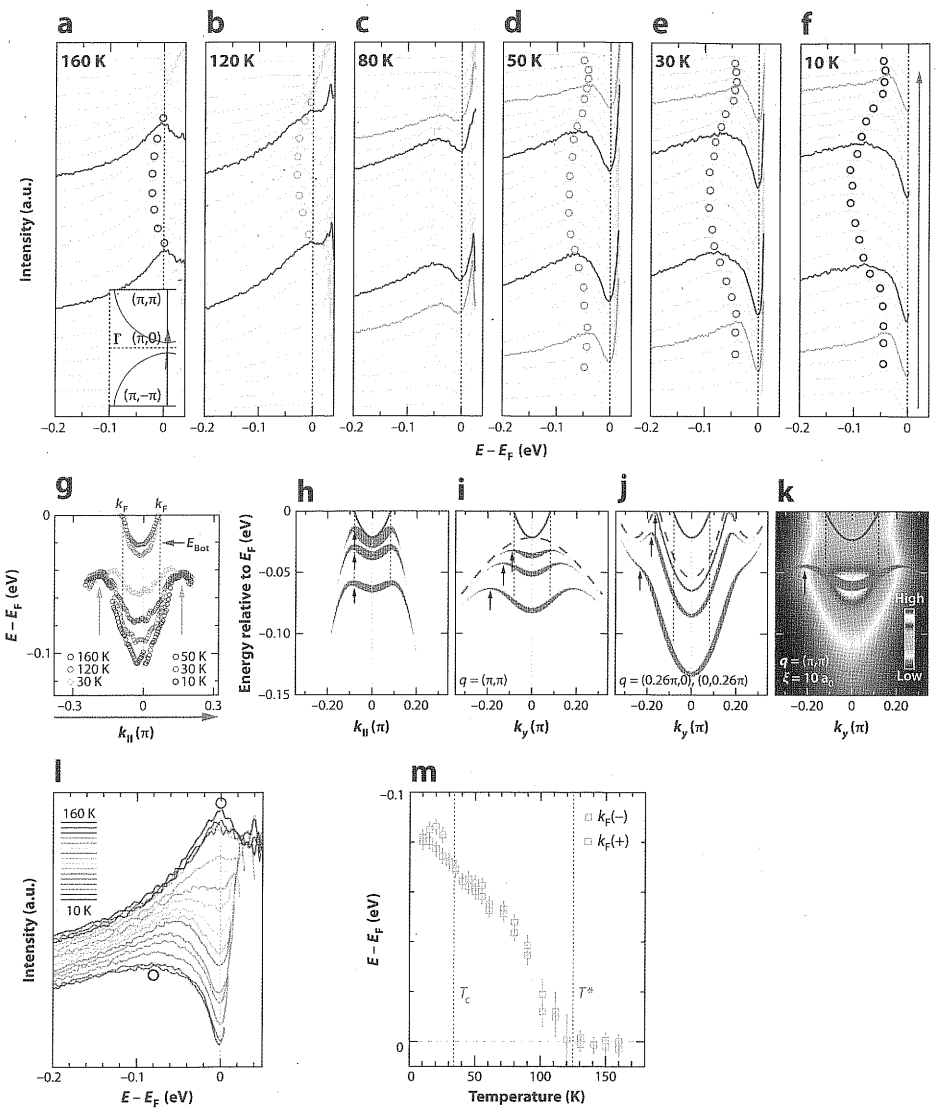

Figure 5

Evidence for particle-hole symmetry breaking in the pseudogap state of Pb-Bi2201 (from Reference 55). (*a–f*) Energy distribution curves (EDCs) along cut shown by blue arrow in the inset of panel *a* from above $T^* = 125 \pm 10$ K to below $T_c = 34$ K. Circles mark EDC peak positions, and red EDCs denote k_F, as defined by Fermi crossing points at 160 K. Light blue EDCs in panels *c–f* define back-bending position, where EDC peak position is closest to E_F. (*g*) Summary of EDC peak positions in panels *a–f*. Light blue arrows denote back-bending positions at the three lowest temperatures and red dotted lines indicate k_F measured at high temperature. (*h*) Simulated dispersion for superconducting gap order parameter $V = 15$, 30, and 60 meV. Back-bending positions marked by black arrows align with the k_F of bare band marked by red dashed lines, reflecting the particle-hole symmetry in the superconducting state. (*i,j*) Simulated dispersions for long-range order density wave with two different q. Green dashed curves are shadow bands from the density wave, which interact with bare bands (*red*) to form renormalized bands (*blue*), with order parameter $V = 15$, 30, and 60 meV. Back-bending positions of renormalized bands in both simulations deviate from k_F, in agreement with experiment. (*k*) Simulated spectra for the (π, π) density wave order with finite correlation length and density wave gap to reproduce the spectral linewidth of experiment. (*l*) Fermi-Dirac divided EDCs at k_F for all temperatures. (*m*) Peak position of EDC at k_F reaches E_F at $T = T^*$.

nominal T^* (**Figure 5*l*,*m***). The observed symmetry change and the temperature dependence are consistent with T^* being a phase transition.

2.4. Outlooks

We have demonstrated how ARPES has contributed to our understanding of superconductivity and strong-correlation physics in the cuprates by investigating the Mott insulating parent compound, electron-boson coupling, and the pseudogap. Whereas the importance of strong electron-correlation is well accepted, polaronic behavior in the parent compound and the phenomenology of the intermediate- and low-energy dispersion kinks suggest that electron-phonon coupling is also an important ingredient to cuprate physics. It remains an open question whether any of these modes are related to a pairing-glue; and if they are not, it is an interesting question why superconductivity can survive amid this strong nonpairing or pair-breaking electron-phonon coupling. Now that there is increasing evidence that the pseudogap is distinct from superconductivity, the remaining challenge is to discern which symmetry the pseudogap breaks, among a myriad of proposals. Finally, a comprehensive understanding of the cuprate problem also requires reconciliation between ARPES and other experiments. One of the most exciting results in the past few years has been the observation of quantum oscillations in the cuprates, particularly $YBa_2Cu_3O_{7-\delta}$, which pointed to a small pocket Fermiology (electron pockets in most experiments), a result not typically seen in ARPES (56, 57). Following this, there have been reports of small hole pockets from ARPES (58, 59), though others have attributed the pocket to structural origins (60). Fluctuating superconductivity above T_c, predicted to be important in systems with reduced dimensionality, has also been of great interest in recent years. Some measurements, particularly Nernst (61) and diamagnetism (62), suggest that fluctuations are present well above T_c, but others, such as terahertz spectroscopy (63) and microwave conductivity (64), suggest they are only significant approximately 10–20 K above T_c. A challenge for ARPES is to disentangle signatures of superconducting fluctuations from pseudogap physics in order to make contributions to this important question.

3. IRON PNICTIDE SUPERCONDUCTORS

In the twenty-five-year journey of high T_c research, continuous searches for new families of superconductors that do not contain copper have been made, leading to the discovery of a number of new superconductors, such as Sr_2RuO_4 (65), MgB_2 (66), and $Na_{0.35}CoO_2 \cdot 1.3H_2O$ (67), etc. However, none of these materials has a T_c high enough to break the monopoly of cuprates as the only family of HTSCs. In February of 2008, the discovery of superconductivity in $LaFeAs(O_{1-x}F_x)$ (68) ignited an explosion of research activities that uncovered a new family of HTSCs based on iron. This family turned out to have an expansive selection of material variations, with the highest T_c reaching 55 K in $Sm(O_{1-x}F_x)FeAs$ (69), thus opening up a new playground toward the ultimate understanding of HTSCs. A common feature of these new iron-based superconductors is a two-dimensional layer of iron and pnictogen or chalcogen atoms in a tetrahedral lattice; hence, these materials became known as iron pnictides and iron chalcogenides. For this review, we focus mostly on iron pnictides, on which the majority of ARPES experiments were performed.

The iron pnictides were soon realized to have a phase diagram analogous to that of cuprates (**Figure 6*a***), with an AFM ground state in the parent compounds, which is separated from the high-temperature paramagnetic state via a collinear SDW transition and an orthorhombic to tetragonal structural transition (70, 71). With either chemical doping or application of pressure,

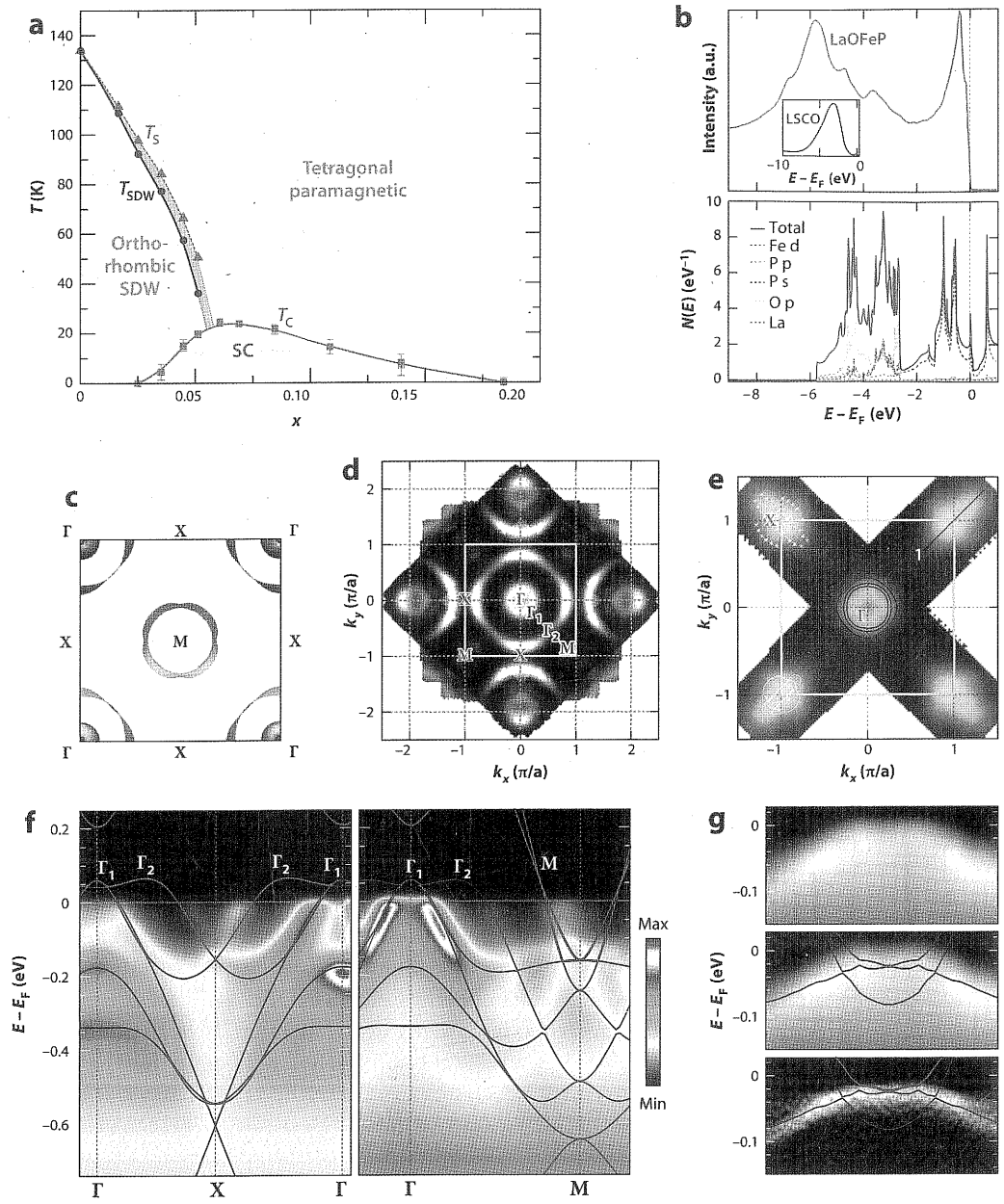

Figure 6

Normal state electronic structure of iron pnictides. (*a*) Phase diagram of a representative iron pnictide family, $Ba(Fe_{1-x}Co_x)_2As_2$. (Adapted with permission from Reference 73. Copyright 2009 by the American Physical Society.) (*b*) Measured angle-integrated photoemission spectrum of LaOFeP compared with the local density approximation (LDA) calculated density of states. Inset shows the valence band of $La_{2-x}Sr_xCuO_4$ (LSCO) for comparison. (*c*) Nonmagnetic LDA calculated Fermi surface (FS). (*d*) Measured FS of LaOFeP. (*e*) Measured FS of $BaFe_2As_2$ at 150 K above T_{SDW}. (*f*) Measured band dispersions of LaOFeP overlaid with LDA calculated bands along two high symmetry cuts. (*g*) Comparison of measured band dispersion of $BaFe_2As_2$ along the red line marked in panel *e* above T_{SDW} and renormalized LDA near the X-point of $BaFe_2As_2$. (Data taken from References 86 and 89.) Abbreviations: SDW, spin density wave; SC, superconductivity.

both SDW and structural transitions are suppressed, eventually allowing the emergence of superconductivity (72–74). To date, those pnictide parent compounds showing such magnetic ground states all seem to have Fe-As layers, such as LnFeAsO (Ln = lanthanides) or 1111, AFe_2As_2 (A = Ba, Sr, Ca) or 122, and NaFeAs or 111. Doping into superconductivity can be achieved by either carrier doping or isovalent substitution of As by P.

In other ways, the iron pnictides contrast with the cuprates. The pnictides are multiband systems, having all five Fe 3*d* bands active near the Fermi level (75), as opposed to the single $d_{x^2-y^2}$ band in cuprates. In this respect, ARPES, with its ability to resolve complex band structure, has proven to be an especially powerful tool for studying the electronic structure of the iron pnictides from a microscopic level. In the following sections, we review some of the ARPES contributions to our understanding of the iron pnictides according to the three regions of the phase diagram—the normal state, the SDW state, and the superconducting state—as well as a brief overview of some doping evolution studies.

3.1. Normal State

The normal state in the iron pnictides refers to the tetragonal paramagnetic state, which spans from the high-temperature region above the SDW and structural phase transitions for the parent compound to the region above the superconducting transition on the OD side (**Figure 6***a*). As this is the state from which the magnetic order and superconductivity emerge, a comprehensive understanding of this state would provide important insights into the origin of the mechanisms that induce the magnetic order and superconductivity.

The rapid development in the investigations of iron pnictides in many ways drew upon the expertise and wisdom developed in the two decades of cuprate research. Immediately following the discovery, two distinct groups of theoretical approaches emerged for describing the ground state of the iron pnictides: local moment AFM ground state for a strong coupling approach based on on-site correlations and proximity to a Mott insulating state and, thus, resemblance to cuprates (76–81); and itinerant ground state for a weak coupling approach emphasizing itinerant electron physics and spin fluctuations (75, 82–85). By studying the electronic structure in the normal state and comparing with the prediction of local density approximation (LDA) calculations, the strength of the correlation can be gauged and the appropriate theoretical starting point determined.

One of the earliest ARPES studies, performed on LaOFeP (86), focused on distinguishing these two theoretical approaches. LaOFeP is a compound effectively on the OD side of the phase diagram with no SDW or structural transition and a T_c of 5.9 K. The angle-integrated photoemission spectrum (**Figure 6***b*) reveals a peak near E_F to be as strong as the valence band (VB) peak, comparable to the high density of states at E_F predicted by LDA calculations. This is in sharp contrast to the observed weak feature near E_F on top of a broad VB peak in the typical VB spectrum of cuprates (*inset* of **Figure 6***b*) that is consistent with the doped Mott insulator picture. Furthermore, the measured FS of LaOFeP shows five bands crossing E_F, forming three hole pockets at the Γ-point and two electron sheets at the (π, π) zone corner (**Figure 6***d*), as predicted by nonmagnetic LDA calculations (**Figure 6***c*). A good agreement can be found between nonmagnetic LDA calculated bands and measured dispersions, after shifting the LDA bands up by 0.11 eV and then renormalizing by a factor of 2.2 (**Figure 6***f*). The shift can be understood as the doping level changes on the cleaved surface due to the lack of a charge neutral cleavage plane (86, 87). The renormalizing factor of 2.2, on the other hand, is comparable to that of Sr_2RuO_4 (88), which is a correlated Fermi liquid well described by theories using itinerant band structure as the starting point. The clear disparity between the VB of pnictides

and cuprates as well as the high degree of agreement between LDA calculations and measured electronic structure suggest that itinerant rather than Mott physics is a more appropriate starting point for LaOFeP.

Subsequent ARPES studies showed that the basic pnictide electronic structure as exemplified in LaOFeP is common across the normal state part of the phase diagram in various material families. In the 122 family, study of the parent compound $BaFe_2As_2$ above T_{SDW} (**Figure 6*e*,*g***) as well as the hole-doped $Ba_{0.6}K_{0.4}Fe_2As_2$ and electron-doped $Ba(Fe_{0.94}Co_{0.06})_2As_2$ also revealed quantitative agreement with LDA calculations (89), albeit with a band renormalization and momentum-dependent shift between the hole bands at Γ and the electron bands at X. Here we note that the multiorbital nature of the pnictides becomes important as the five Fe 3*d* bands near E_F have distinct orbital symmetries, which are subject to photoemission matrix elements that enhance or suppress the intensity of corresponding bands differently under different light polarizations (5). This was experimentally shown (89, 90) to be responsible for the suppression of electron bands at the X-point in early ARPES studies (91). The momentum-dependent shift between the hole and electron bands is also seen in subsequent quantum oscillation measurements (92), and could be an indication of correlation effects such as interband coupling unaccounted for in oversimplified LDA calculations (89, 93, 94). Nevertheless, the large overall agreement between observed electronic structure and LDA calculations across the wide region of the normal state favors the itinerant band approach as the appropriate starting point for describing the fundamental properties of the pnictides.

3.2. Spin-Density-Wave State

For cuprates, ARPES studies of the parent compounds have played an important role in formulating the correct theoretical models for the description of Mott physics in the UD regime. For iron pnictides, the nature of the magnetism in the parent compounds, whether dictated by local moment physics or dominated by itinerant character, remains a controversial issue. It is interesting to observe that in the large material base of the iron pnictides, almost all those capable of being doped into HTSCs have the collinear SDW and structural transition in the UD region, whereas those that do not have such competing phases (i.e., phosphides as opposed to arsenides) have maximum T_c's of only a few Kelvin. This intriguing proximity of the competing phases to HTSCs makes it especially compelling to characterize the electronic structure of the SDW state.

In this regard, there has been a long struggle in the ARPES community to understand the nature of the electronic structure in the SDW state, partly due to its extreme complexity and lack of adequate theoretical calculations for the magnetically ordered ground state. Although the data taken in the normal state above the SDW transition (**Figure 7*a*,*e***) match well with LDA band structure calculations as discussed in the previous section, the data taken in the SDW state reveal a complex electronic reconstruction across the SDW transition (**Figure 7*b*,*f***). Most obvious is the addition of small side pockets around the Γ-point, where only concentric hole pockets at Γ exist in the normal state. Another apparent difference is the appearance of very bright spots along the Γ-X high-symmetry direction close to the X-point. Such dramatic electronic reconstruction has been reported in various pnictide compounds, including 1111 compounds (95) and 122 compounds (90, 96–101), as well as 111 compounds (102). As the SDW transition breaks translational symmetry by introducing a $\sqrt{2} \times \sqrt{2}$ Brillouin zone (BZ) folding, one may expect the reconstructed electronic structure to be the result of a direct folding of the normal state dispersion between the Γ and X via the SDW ordering vector (π, π). However, considerations of such a folding scenario are not able to reproduce the observed

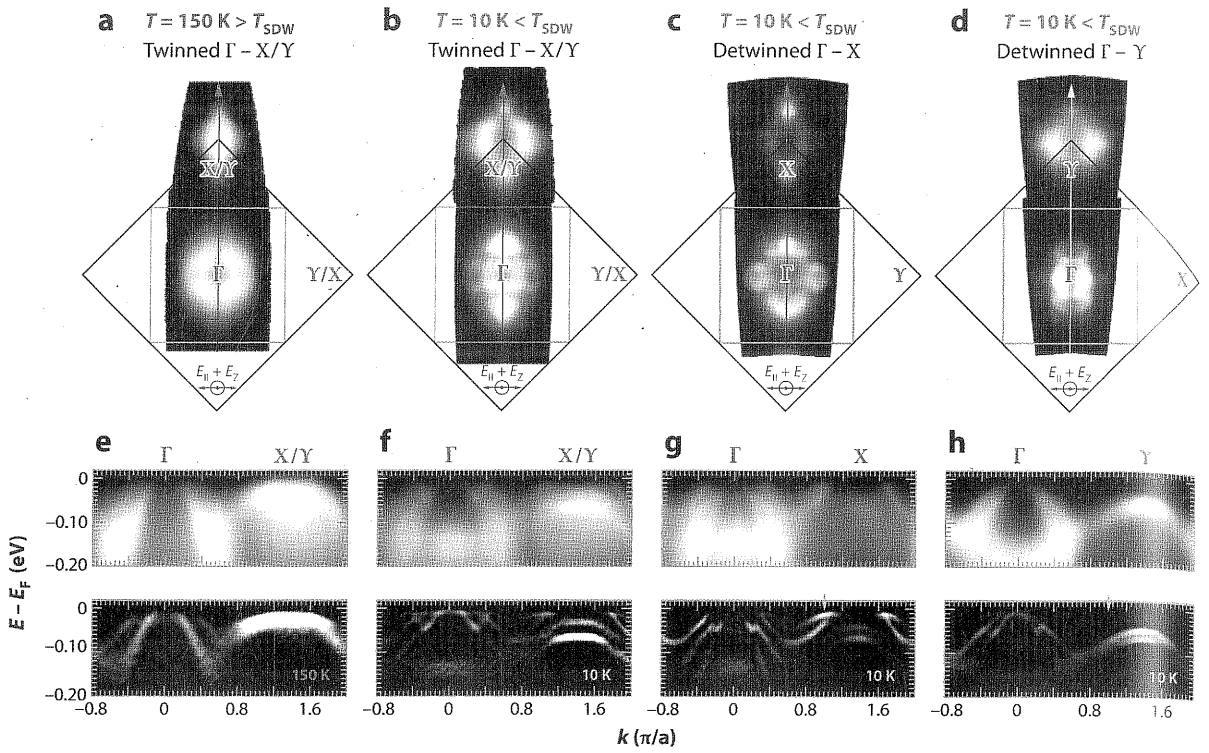

Figure 7

Electronic reconstruction across T_{SDW} measured on twinned and detwinned $BaFe_2As_2$. (*a*) Fermi surfaces (FS) taken in the tetragonal paramagnetic state (150 K). (*b*) FS taken in the SDW state (10 K) on twinned crystal. (*c,d*) FS taken in the SDW state (10 K) on detwinned crystal along the Γ-X and Γ-Y directions, respectively. (*e–h*) Corresponding spectral images along the marked high-symmetry directions. All data taken with 25-eV photons. (Data taken from References 96 and 105.)

complexity in the SDW state, not even the total number of observed bands (96). Various proposals have been put forward to interpret the complex electronic structure measured by ARPES, including an exotic exchange splitting scenario (97), an anisotropic SDW gap picture (90), and an empirical fit by LDA calculations with fixed magnetic moment (96). Although each proposal captures certain aspects of the experimental results, none of them provides a comprehensive and insightful description of the electronic structure evolution across the SDW transition.

Part of the complication arises from the existence of natural twin domains below T_s due to the development of lattice orthorhombicity (103, 104), resulting in domain mixing in the ARPES signal. Recent ARPES measurements on mechanically detwinned $Ba(Fe_{1-x}Co_x)_2As_2$ crystals (105) reveal that the intrinsic single-domain electronic structure in the SDW state has broken C_4 rotational symmetry between the AFM (Γ-X) and FM (Γ-Y) directions (**Figure 7***c,d,g,h*), respecting the lowered in-plane symmetry of both the crystal and spin structures below T_{SDW}. This electronic anisotropy is observed in both the FS and band dispersions. The most anisotropic feature from these orthogonal directions are the dominant hole-like dispersions near the X and Y points, as marked in purple and red in **Figure 8***a,b*, with one crossing E_F and the other sitting well below. The consideration of polarization matrix elements further reveals that the band along Γ-X is of dominant d_{yz} character, whereas the band along Γ-Y is of

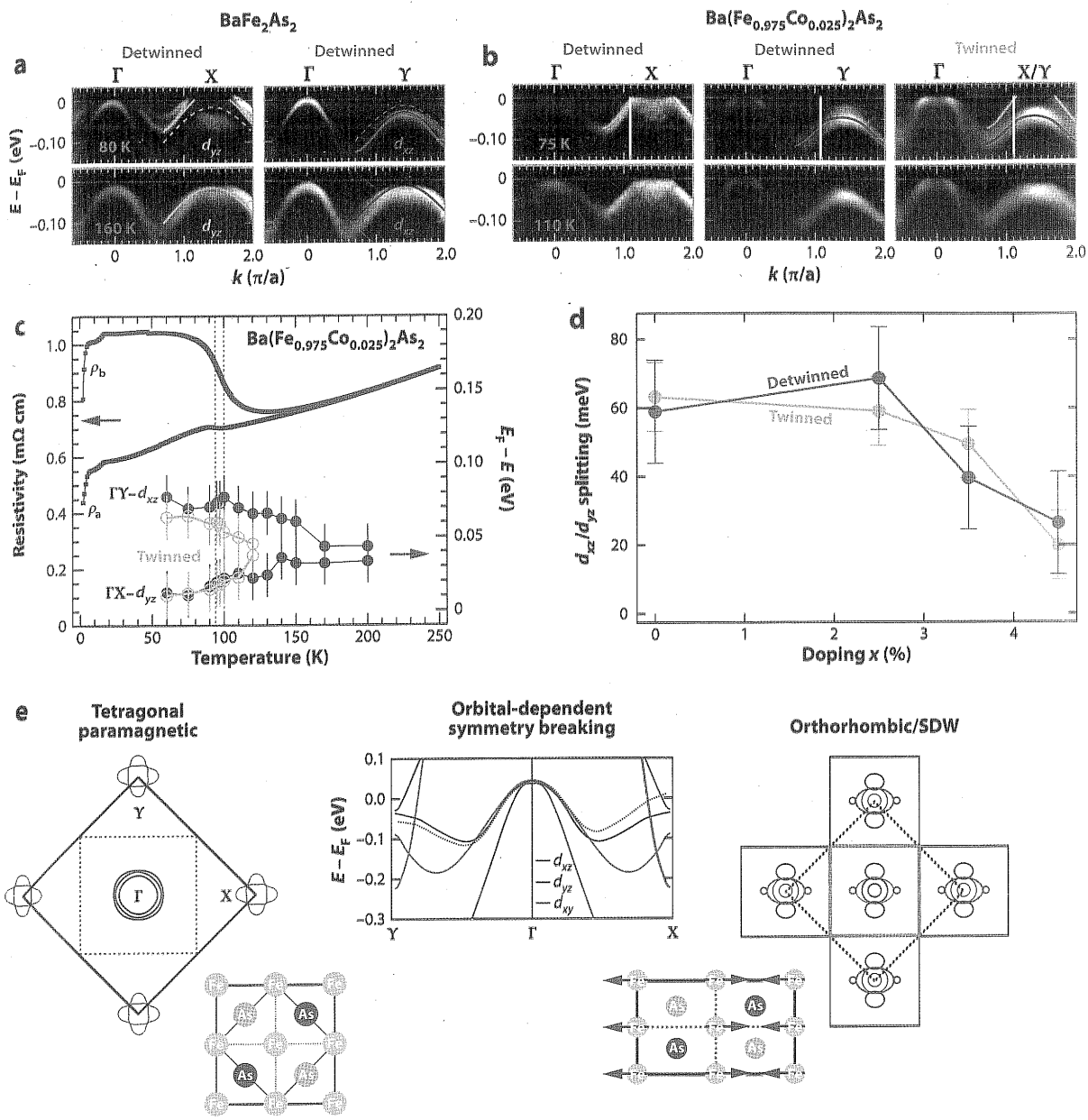

Figure 8

Electronic anisotropy of $Ba(Fe_{1-x}Co_x)_2As_2$. (*a*) High-symmetry cuts taken along Γ-X [antiferromagnetic (AFM)] and Γ-Y [ferromagnetic (FM)] directions of detwinned parent compound (x = 0), above and below T_{SDW} (=138 K). (*b*) Similar measurements taken on detwinned and twinned doped sample (x = 0.025). (*c*) Temperature dependence of energy shift of the d_{yz} (*purple*) and d_{xz} (*red*) bands as measured at the momentum position marked as yellow lines in panel *b*, compared with resistivity measurements reproduced from Reference 104. (*d*) Doping dependence of the d_{xz}/d_{yz} band splitting taken at 10 K. (Data taken from Reference 105.) (*e*) Schematic of development of electronic anisotropy. The band structure is C_4 rotationally symmetric in the tetragonal paramagnetic state. Below T_s, d_{yz} band along Γ-X and d_{xz} band along Γ-Y shifts anisotropically, resulting in the anisotropic electronic structure observed in the low-temperature SDW state.

dominant d_{xz} character. Hence, the anisotropy is also manifested in the orbital degree of freedom. This observation of electronic anisotropy provides a microscopic basis for the many signs of in-plane anisotropy reported in the literature (104, 106, 107).

As the SDW phase has a collinear spin structure that has a C_2 symmetry, one may expect symmetry breaking in the electronic structure as a trivial consequence of the anisotropic spin structure. However, temperature dependence study shows this electronic anisotropy to onset slightly above T_{SDW} in detwinned parent compound where $T_{SDW}=T_S$ and well above T_{SDW} in doped compound where $T_S>T_{SDW}$ (**Figure 8***c*), which is consistent with the observation of in-plane anisotropy in resistivity above T_{SDW} in detwinned crystals (104). Although crystal C_4 symmetry is also broken at T_S with the appearance of lattice distortion, the small magnitude of the orthorhombicity is too small to fully account for the large magnitude of the observed energy splitting of the d_{yz} and d_{xz} bands. This observation of orbital anisotropy above T_{SDW} alone does not distinguish the origin of the structural phase transition, which has been discussed in terms of both spin fluctuations (80, 81, 108) and orbital order (109–111). However, we note that the large amplitude of the band splitting does draw attention to the possibility that the orbital degree of freedom might play an important role.

A doping dependence study (**Figure 8***d*) further shows that the magnitude of the anisotropic splitting decreases monotonically with doping, a trend consistent with the suppression of the magnetic ordering temperature and structural distortion. However, the temperature window above T_{SDW} in which anisotropy persists, which indicates the involvement of fluctuations, appears to be bigger for doping levels closer to the superconducting dome; this is a trend also seen in transport measurements, suggesting that fluctuation effects, possibly of orbital origin, may play an important role in high temperature superconductivity in the iron pnictides.

3.3. Superconducting State

In the study of HTSCs, elucidating the pairing symmetry and mechanism for superconductivity is certainly the central and ultimate goal. More than two decades after the discovery of high T_c cuprates, the pairing mechanism for HTSCs still remains the biggest challenge. In the case of iron pnictides, from a very early stage, the phonon mechanism was theoretically shown to be unlikely (112), and proposals were put forth arguing for an unconventional sign reversal $s\pm$ order parameter (82). As the pnictides are on the verge of a magnetic instability in the UD regime, nesting-induced AFM spin fluctuations are suggested to be the mediator for superconductivity, in the form of an isotropic s wave, albeit with sign reversal between the Fermi pockets at Γ and (π, π). However, early experimental probes by other techniques on different pnictide compounds have reported both nodeless gap (113, 114) and line nodes in the gap (115, 116). Later, motivated by the empirical observation that T_c correlates with the Fe-As-Fe bond angle among pnictide families (117), theoretical work by Kuroki et al. (118) pointed out that the FS character is very sensitive to the pnictogen height, which varies with doping and materials. This parameter could potentially act as a possible switch between high-T_c nodeless and low-T_c nodal pairings in the pnictides. Here, we review some of the ARPES contributions in this regard.

Owing to the lack of a charge neutral cleavage plane in 1111 materials, which effectively changes the doping of the measured surface, most ARPES gap measurements have been focused on 122 compounds. Early measurements on hole-doped $Ba_{0.6}K_{0.4}Fe_2As_2$ (T_c = 37 K) showed nodeless isotropic gap sizes on the three resolvable FSs, with the smaller hole pocket and electron pocket having a 12-meV gap, and the bigger hole pocket having a smaller 6-meV gap (**Figure 9***a*) (119). This is consistent with the $s\pm$ pairing symmetry with a gap function proportional to $|\cos k_x \cos k_y|$. As the 122 compounds are found to be more three dimensional (3D)

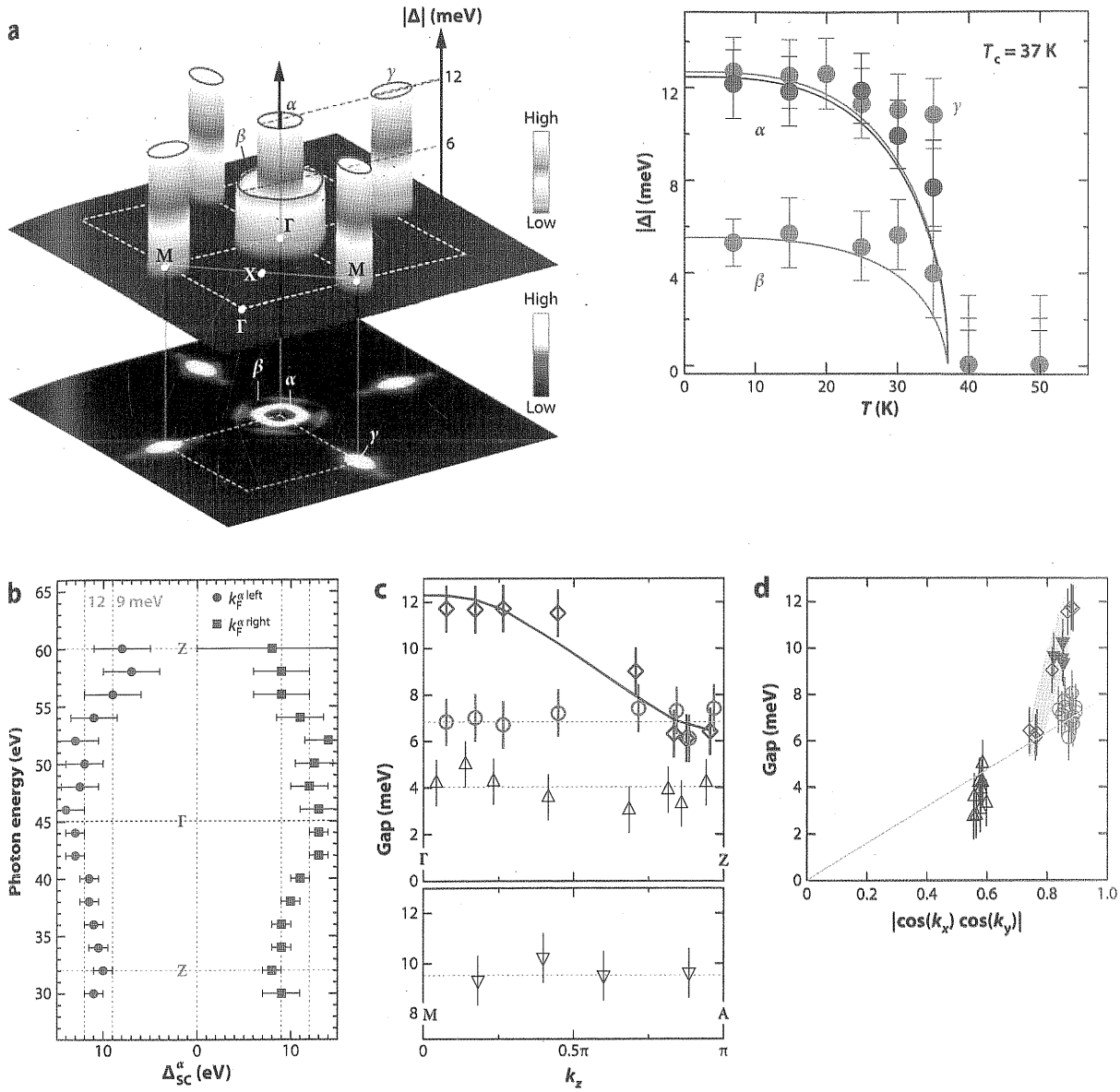

Figure 9

Superconducting gap measurement on $Ba_{0.6}K_{0.4}Fe_2As_2$. (*a*) In-plane gap measurement adapted with permission from Reference 119. (*b*) k_z dependence of gap measured on the inner hole pocket at Γ. [Reprinted by permission from Reference 121. Copyright 2011 Macmillan Publishers Ltd,]. (*c,d*) k_z dependence of gap measurement. (Reprinted with permission from Reference 120. Copyright 2010 by the American Physical Society.)

than 1111 and 111, more detailed ARPES measurements were conducted exploring the 3D character of the gap structure on this compound (**Figure 9*b–d***). A third expected hole band around the Γ-point was resolved via polarization dependence studies (120). A large k_z variation of the superconducting gap was found on one of the hole bands around the Γ-point (120, 121),

which cannot be fully accounted for by the in-plane $s\pm$ gap function proposed so far; this calls for a more complete 3D model for describing the pairing symmetry in the pnictides. More recently, a detailed ARPES measurement (122) on $BaFe_2(As_{0.7}P_{0.3})_2$ (T_c = 30 K) reported a circular line node on the largest hole pocket around the Z-point at $k_z = \pi$, which appears to be consistent with a theoretical prediction for this superconductor (123). The complexity of the superconducting gap structure revealed in this study, along with previous measurements on other pnictide families, demonstrates the strong material dependence of the superconducting gap in iron pnictides. It highlights the critical role of the multiorbital character and three dimensionality of the underlying electronic structures in determining the superconducting pairing symmetry in this new family of HTSCs.

3.4. Doping Evolution

Preliminary studies on the doping evolution of the superconducting gap have also been reported. For the electron-doped side, an ARPES study (124) on $Ba(Fe_{1-x}Co_x)_2As_2$ observed that while both the hole pockets at Γ and the electron pockets at X have finite size at optimal superconducting doping, the hole pockets at Γ disappeared completely as the corresponding hole bands sink below E_F in an OD nonsuperconducting compound. It has been proposed that FS nesting–induced AFM spin fluctuations are responsible for mediating superconductivity in the pnictides. This observation was taken as strong support for the idea that the coexistence of hole and electron pockets connected via the AFM wave vector (π, π) is essential in realizing the mechanism of superconductivity in the iron-based superconductors (**Figure 10*a***).

On the hole-doped side, ARPES study (125) on $Ba_{1-x}K_xFe_2As_2$ confirmed a nodeless isotropic gap that is universal across the phase diagram. In addition, the ratio of the gap size to T_c ($2\Delta/k_BT_c$) for each FS was found to remain more or less constant for each FS pocket over a wide doping range (**Figure 10*b***). However, the gap magnitudes on different sheets of FS seem to deviate from a simple $|\cos k_x \cos k_y|$ functional form in the OD case, as the electron pockets are much smaller than the inner hole pocket though their gap sizes are comparable. Hence, an additional term proportional to $|\cos k_x + \cos k_y|$, which was argued to be induced by the next-nearest-neighbor pairing, was introduced to resolve the discrepancy and obtain a better fit by a single gap function that is consistent with the $s\pm$-wave pairing. Furthermore, the observation of significant mismatch between the small electron pockets and large hole pockets in the OD $Ba_{1-x}K_xFe_2As_2$ suggests that FS overlapping is not strictly required for superconductivity in the pnictides.

Regarding the evolution from the magnetic ground state to the superconducting regime, a doping-dependent ARPES study of the UD region of the $Ba(Fe_{1-x}Co_x)_2As_2$ series reports a Lifshitz transition at the onset of superconductivity (101). In this study, the bright spots observed on the FS in the SDW state are attributed to the folding of hole bands at Γ and electron bands at X, which opens a small gap near E_F in the parent compounds, forming small hole pockets around the X-point. With electron doping, the small hole pockets are expected to disappear below E_F as the chemical potential shifts up into the gap, leading to a Lifshitz transition, which coincides with the onset of superconductivity in this doping series (**Figure 10*c–e***). However, this claim is mostly based on a series of FS mappings along with a simple model simulation. There is no direct evidence for the existence of such a small gap in the corresponding band dispersion. In this respect, a small hybridization gap proposed in this paper is inconsistent with the ARPES results on detwinned $Ba(Fe_{1-x}Co_x)_2As_2$ (105), in which the two bands sketched in **Figure 10*e*** are identified to have orbital characters with opposite symmetry; hence, they cannot hybridize along the high symmetry lines. The disappearance of the bright